A Self-Calibration Bundle Adjustment Method for Photogrammetric Processing of Chang′E-2 Stereo Lunar Imagery

Kaichang Di, Yiliang Liu, Bin Liu, Man Peng, and Wenmin Hu

***Abstract*—Chang′E-2 (CE-2) lunar orbiter is the second robotic orbiter in the Chinese Lunar Exploration Program. The charge-coupled-device (CCD) camera equipped on the CE-2 orbiter acquired stereo images with a resolution of less than 10 m and global coverage. High-precision topographic mapping with CE-2 CCD stereo imagery is of great importance for scientific research, as well as for the landing preparation and surface operation of the incoming Chang′E-3 lunar rover. Uncertainties in both the interior orientation (IO) model and exterior orientation (EO) parameters of the CE-2 CCD camera can affect mapping accuracy. In this paper, a self-calibration bundle adjustment method is proposed to eliminate these effects by adding several parameters into the IO model and fitting EO parameters using a third-order polynomial. The additional IO parameters and the EO polynomial coefficients are solved as unknowns along with ground points in the adjustment process. A series of strategies is adopted to ensure the robustness and reliability of the solution. Experimental results using images from two adjacent tracks indicated that this method effectively reduced the inconsistencies in the image space from approximately 20 pixels to subpixel. Topographic profiles generated using unadjusted and adjusted CE-2 data were compared with Lunar Orbiter Laser Altimeter data. These comparisons indicated that the local topographies generated after bundle adjustments, which reduced elevation differences by 9–10 m, were more consistent with LOLA data.**

***Index Terms*—Chang′E-2 stereo imagery, self-calibration bundle adjustment (SCBA), topographic mapping.**

I. Introduction

SINCE the 1990s, a new series of lunar explorations have emerged, and spacecraft equipped with high-technology scientific instruments have been successively launched. As the most important and basic equipment for topographic and morphological mapping, the optical cameras carried by these spacecraft acquired numerous high-resolution lunar images, such as Clementine [1], SELENE [2], Chandrayaan-1 [3], and Lunar Reconnaissance Orbiter (LRO) [4]. China also conducted its robotic lunar exploration program (Chinese Lunar Exploration Program), which is commonly known as the Chang′E program. This program has three phases, namely, orbital mission, soft lander and rover, and automated sample return [5]. Change′E-1 (CE-1) and Chang′E-2 (CE-2) are the orbiters in phases I and II, respectively.

The CE-1 orbiter was launched on October 24, 2007 with a three-line-array push-broom charge-coupled-device (CCD) camera and a laser altimeter (LAM) for acquiring global lunar CCD images with a 120-m resolution and LAM data at 1400-m along-track spacing, producing a global image mosaic of the Moon [5], [6]. After the general survey by the CE-1 orbiter, the CE-2 orbiter (launched on October 1, 2010) conducted a global survey of the lunar surface with a higher resolution and more detailed investigations on the certain regions of interest, such as the preselected landing site of the Chang′E-3 (CE-3) lander and rover [7]. As a follow-up orbiter of CE-1, CE-2 is similar in design to CE-1 but has significant technical improvements such as a high-resolution CCD camera that can capture images with a resolution 17 times higher than those captured by CE-1. A local image map of Sinus Iridum, the preselected landing site of CE-3 lunar rover, which was produced using CE-2 CCD images, was released on November 8, 2010 [8]. A global image mosaic of the Moon with 7-m resolution was also released by the State Administration for Science, Technology and Industry for National Defense on February 6, 2012 [9].

Considering the systematic errors usually caused by orbit position and orientation errors, unstable relationship of CCD camera line arrays, and so on, adjusting the lunar orbital data is necessary and critical to produce high-precision topographic maps. Considerable effort has been exerted toward developing adjustment methods for lunar and Mars imagery. A method for adjusting the nominal camera pointing and spacecraft trajectory data was used in the Clementine Ultraviolet/Visible multilook angle images [10]. Haruyama *et al.* corrected the distortion models of TC CCD detectors and attachment angles of TC telescopes in SELENE mission to produce a lunar global digital terrain model [11]. Radhadevi *et al.* generated digital elevation models (DEMs) and orthoimages from Chandrayaan-1 TMC stereo triplets through various operations such as modeling camera trajectory, sensor modeling, automatic tie point/check point/lunar control point identification, block adjustment, image matching, and stereo intersection [12]. ASU, DLR/TUB, UA, USGS, OSU, and Ames adopted different software packages and methods to generate high-precision topographic

Manuscript received February 17, 2013; revised August 28, 2013 and October 10, 2013; accepted October 22, 2013. This work was supported in part by the National Key Basic Research and Development Program of China under Grant 2012CB719902 and in part by the National Natural Science Foundation of China under Grant 41171355 and 41201480.

The authors are with the State Key Laboratory of Remote Sensing Science, Institute of Remote Sensing and Digital Earth, Chinese Academy of Sciences, Beijing 100101, China (e-mail: kcdi@irsa.ac.cn; ylliu@irsa.ac.cn; liub@irsa.ac.cn; pengman@irsa.ac.cn; huwm@irsa.ac.cn).

Color versions of one or more of the figures in this paper are available online at http://ieeexplore.ieee.org.

Digital Object Identifier 10.1109/TGRS.2013.2288932

0196-2892 © 2013 IEEE. Personal use is permitted, but republication/redistribution requires IEEE permission.
See http://www.ieee.org/publications_standards/publications/rights/index.html for more information.

products using LRO narrow-angle camera data by boresight calibration, bundle adjustment (BA), and so on [13], [14]. Similar adjustment processing methods were also used in Mars topographic mapping using the Mars Orbiter Camera, Mars Orbiter Laser Altimeter, High-Resolution Stereo Camera, and High-Resolution Imaging Science Experiment data [15]–[19].

With a gradual release of Chang′E (CE) data, many researchers focus their attention on the geometric modeling and adjustment processing of CE data. Wang adopted an equivalent frame photo bundle adjustment method, which regards short-time push-broom imaging as frame imaging, to perform close fitting and adjustment calculation for CE-1 CCD images [20]. Peng *et al.* developed a rigorous sensor model of the CE-1 CCD camera, through which a high-precision DEM was automatically generated [21]. Based on the push-broom imaging principle, Di *et al.* implemented a 3-D registration of the CE-1 CCD images and LAM data [22]. Wu *et al.* presented a combined adjustment method with both CE-1 CCD images and LAM data [23]. Furthermore, Di *et al.* improved the coregistration algorithm of LAM points and CCD images through LAM crossover adjustment and image sensor model refinement [24].

For CE-2, no LAM data were acquired. Thus, CE-2 CCD images are the only available data from the mission for topographic mapping. Since the CE-2 images cover the entire lunar surface and have the highest resolution (7-m resolution) among the global lunar image data sets at present, it is valuable and critical to study the rigorous geometric modeling and high-precision processing of CE-2 CCD images. CE-2 has different characteristics from existing planetary or Earth observation satellites in terms of orbit design, orbit determination uncertainty, and imaging sensor configuration. So far, geometric modeling and processing of CE-2 CCD images have not been systematically investigated yet. In our previous work, a rigorous geometric CE-2 CCD camera model was developed, and a simple adjustment method was used to reduce the inconsistencies between forward- and backward-looking images in one track. DEM and digital orthophoto map (DOM) for partial CE-2 CCD images were generated [25]. However, this method did not consider orbit position and orientation errors and was only applied to stereo imagery mapping in one track. It is necessary to develop and publish a rigorous adjustment method for multitrack CE-2 CCD image processing and mapping.

Unlike the CE-1 CCD camera implemented on an area array CCD sensor [26], the two line arrays of the CE-2 CCD camera [26]–[28] are separately assembled on a focal plane to constitute a relatively unstable structure, which may cause internal inconsistencies. Thus, the effect of the camera's interior relationship on mapping accuracy should not be neglected, and previous adjustment methods used for CE-1 CCD images, which only focus on the refinement of exterior orientation (EO) parameters, are insufficient to be applied to CE-2 CCD images. Furthermore, we determined through an extensive analysis of the original telemetry data that the quality of CE-2 orbiter's attitude data (pointing data) cannot meet the requirements of high-resolution topographic mapping (which would be elaborated later). Thus, a new method that can adjust the interior orientation (IO) model and EO parameters simultaneously without the original attitude data is the focus of this paper.

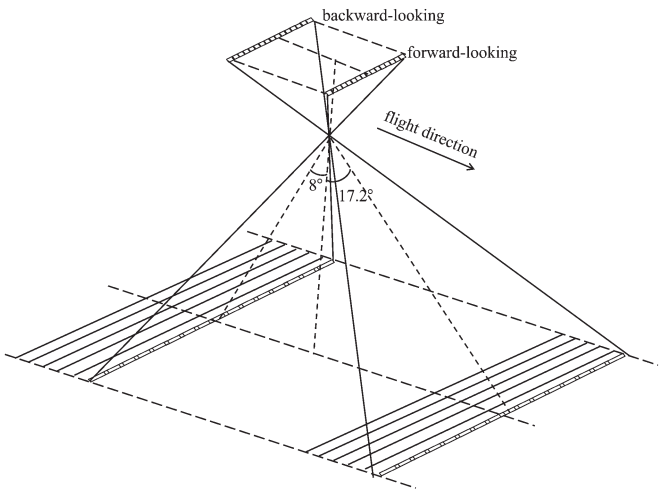

Fig. 1. CE-2 stereo camera imaging configuration.

In this paper, we present a self-calibration bundle adjustment (SCBA) method (also called overall adjustment with additional parameters) to refine the spatial relationship between the two CCD camera line arrays and the EO parameters. First, a rigorous geometric model (including the IO and EO models) of the CE-2 CCD images is developed. Second, hundreds of tie points evenly distributed in the overlapping area are selected and used to generate the corresponding ground points as initial adjustment values. Third, the IO model is modified by adding several parameters, and the EO parameters are fitted using a third-order polynomial; the additional parameters and polynomial coefficients are incorporated into the BA equations as unknowns along with the ground points. Finally, the DEM and DOM at Sinus Iridum are generated using the refined IO model and EO parameters. The accuracy in image space is evaluated by calculating residuals before and after adjustment; the accuracy in object space is verified by comparing the DEMs with two Lunar Orbiter Laser Altimeter (LOLA) data tracks. The adjustment results using a BA method without self-calibration (traditional BA) are also listed for comparison purposes.

II. Rigorous Geometric Model of CE-2 CCD Images

A. Overview of CE-2 CCD Camera

As shown in Fig. 1, the CE-2 CCD stereo camera adopts a stereo imaging solution with a single lens and two look angles in the same track and a push-broom imaging mode with high-sensitivity time-delay integration CCD [27]. It acquires images at two different orbit heights: One is a 100 km $\times$ 100 km circular orbit to provide high-resolution global image coverage of the Moon for various scientific research studies, and the other is a 100 km $\times$ 15 km elliptical orbit to provide more detailed information for the CE-3 rover landing and surface operation. Images acquired at these two orbit heights can reach a resolution of around 7m and 1.5 m (at the perilune) [26].

The CE-2 CCD camera consists of two line arrays that are separately fixed on the focal plane. The two arrays share the same optical axis with a focal length of 144.3 mm. Each line array has 6144 pixels. The primary technical parameters are listed in Table I [26].

TABLE I
TECHNICAL PARAMETERS OF CE-2 CCD CAMERA

Parameters	Orbit	
	100 km circular orbit	100×15 km elliptical orbit
Image Swath	≥43 km	≥6 km
Spatial resolution	≤10 m	≤1.5 m
Look angle	Forward-looking +8°, backward-looking -17.2°	
Focal Length	144.3mm	

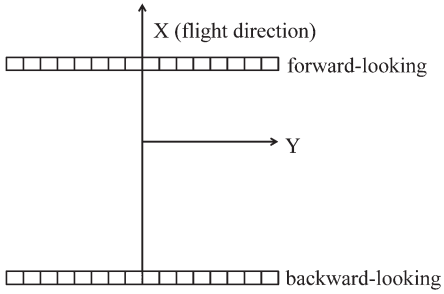

Fig. 2. Focal plane of CE-2 CCD camera.

B. Interior Orientation (IO)

IO refers to the transformation from the image space coordinate system (ISCS) to their focal plane coordinate system (FPCS) centered at the principal point of the image according to the calibrated IO parameters of the camera. Fig. 2 shows the focal plane structure of the CE-2 CCD camera; the X-axis of the FPCS represents the flight direction and is perpendicular to the two line arrays. According to the definition of FPCS, the IO model of the CE-2 CCD camera can be derived using

$$\begin{aligned} x &= x_0 - \tan(\theta) \cdot f \\ y &= y_0 - (col - s_0) \cdot pixsize \end{aligned} \tag{1}$$

where θ represents the look angle, which is 8° for forward-looking images and -17.2° for backward-looking images; f denotes the focal length; col is the column number (image coordinate) of an image point; s_0 is the CCD center, the value of which is 3071.5; *pixsize* stands for the pixel size of the CCD array, which is 10.1 μm [28]; (x_0, y_0) represents the principal point position in the focal plane frame; and (x, y) are the focal plane coordinates of forward- or backward-looking images.

C. Exterior Orientation (EO)

EO refers to the transformation between the FPCS and lunar body-fixed coordinate system (LBF). The rigorous geometric model can be represented as collinearity equations as either of the following:

$$\begin{aligned} x &= -f\frac{a_1(X-X_s)+b_1(Y-Y_s)+c_1(Z-Z_s)}{a_3(X-X_s)+b_3(Y-Y_s)+c_3(Z-Z_s)} \\ y &= -f\frac{a_2(X-X_s)+b_2(Y-Y_s)+c_2(Z-Z_s)}{a_3(X-X_s)+b_3(Y-Y_s)+c_3(Z-Z_s)} \end{aligned} \tag{2}$$

$$\begin{bmatrix} X-X_s \\ Y-Y_s \\ Z-Z_s \end{bmatrix} = \lambda \mathbf{R_{ol}} \mathbf{R_{bo}} \mathbf{R_{ib}} \begin{bmatrix} x \\ y \\ -f \end{bmatrix} = \lambda \mathbf{R} \begin{bmatrix} x \\ y \\ -f \end{bmatrix} \tag{3}$$

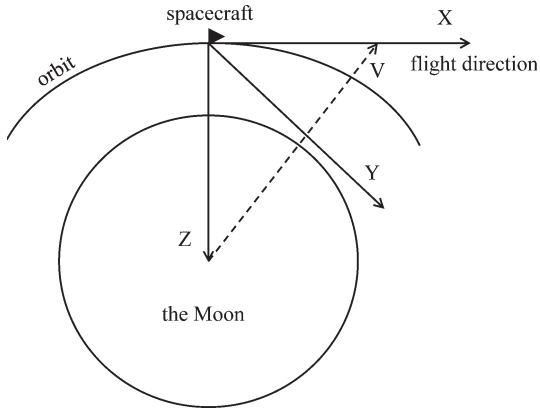

Fig. 3. Orbit coordinate system definition.

where (x, y) are the focal plane coordinates of an image point; f is the focal length; (X, Y, Z) and (Xs, Ys, Zs) are the ground point and the perspective center position in LBF, respectively; $\mathbf{R_{ib}}$ is the rotation matrix from the ISCS to the spacecraft body coordinate system (BCS); $\mathbf{R_{bo}}$ is the rotation matrix from the BCS to the orbit coordinate system (OCS); $\mathbf{R_{ol}}$ is the rotation matrix from the OCS to the LBF; λ is a scale factor; $\mathbf{R}$ represents the overall rotation matrix from the ISCS to the LBF; and a_i, b_i, and c_i $(i = 1, 2, 3)$ are the elements of rotation matrix $\mathbf{R}$.

The $\mathbf{R_{ib}}$ matrix is also called the placement matrix, which is a constant matrix that approximates to a unit matrix. $\mathbf{R_{bo}}$ is calculated from the original attitude data. $\mathbf{R_{ol}}$ is calculated using the interpolated orbiter's ephemeris data (including the position and velocity of the spacecraft in the LBF) and attitude data (including the three Euler angles from the BCS to the OCS).

This paper only discusses the 100 km × 100 km circular orbit. Fig. 3 shows the OCS, the origin of which is at the spacecraft's center of mass. The Z-axis of OCS points to the Moon's center of mass; its X-axis is in the orbital plane, perpendicular to the Z-axis, and pointing forward, whereas its Y-axis is perpendicular to the orbit [29]. Based on the position vector (X_s, Y_s, Z_s) (Z-axis) and the velocity vector (dx, dy, dz), the Z-, Y-, and X-axis vectors of the OCS in the LBF can be determined as follows:

$$\begin{aligned} \mathbf{Z_{axis}} &= [\, X_s \quad Y_s \quad Z_s \,]^T \\ \mathbf{v} &= [\, dx \quad dy \quad dz \,]^T \\ \mathbf{Y_{axis}} &= \mathbf{Z_{axis}} \times \mathbf{v} \\ \mathbf{X_{axis}} &= \mathbf{Y_{axis}} \times \mathbf{Z_{axis}} \end{aligned} \tag{4}$$

where $\times$ stands for the cross product of two vectors. Thus, $\mathbf{R_{ol}}$ is calculated using

$$\mathbf{R_{ol}} = \left[\, \frac{\mathbf{X_{axis}}}{|\mathbf{X_{axis}}|} \quad \frac{\mathbf{Y_{axis}}}{|\mathbf{Y_{axis}}|} \quad \frac{\mathbf{Z_{axis}}}{|\mathbf{Z_{axis}}|} \,\right]. \tag{5}$$

Therefore, a rigorous geometric model is established to implement the transformation between the focal plane coordinates and the ground coordinates in the LBF.

For push-broom sensors, each image scan line should have a specific set of EO parameters $(X_s, Y_s, Z_s, \varphi, \omega, \kappa)$, but the acquisition frequency of the original telemetry (spacecraft positions and attitudes) is much lower than that of the image scanning. Thus, we use a polynomial model to interpolate the EO parameters for each scan line (as elaborated in Section III). (X_s, Y_s, Z_s) can be directly interpolated using the ephemeris in the LBF, and the three Euler angles $(\varphi, \omega, \kappa)$ from the BCS to the OCS can be interpolated from the angles calculated from matrix $\mathbf{R_{ol}R_{bo}}$.

D. Space Intersection and Back Projection

The forward- and backward-looking images in one track or the images from adjacent tracks can form stereo pairs for 3-D topographic mapping. After a series of image processing (including image stretching for enhancing image contrasts, scale-invariant feature transform (SIFT) matching [30] for obtaining tie points, random sample consensus (RANSAC) algorithm [31] for eliminating gross errors, and dense matching for obtaining dense homologous points), 3-D ground points are calculated by space intersection. Subsequently, the DEM is generated by interpolating the dense ground points. In this paper, a least square solution using linearized collinearity equations based on the rigorous sensor model is adopted to obtain the ground points.

Given the 3-D ground points and the rigorous geometric model, we can obtain the back-projected image points corresponding to the tie points for each image. Back-projection residuals between the back-projected points and the tie points are calculated to measure the consistency in image space. The image space residual is an important indicator for the accuracy of IO and EO parameters.

Considering the various error sources, the accuracy of original EO parameters derived from telemetry data is typically inadequate. Moreover, the calibrated IO parameters may slightly change during orbit over time. Therefore, the calculated 3-D ground positions are not accurate enough and are not consistent between adjacent tracks. Achieving higher mapping accuracy requires the adjustment of the EO and IO parameters to reduce the errors, including systematic and random errors.

III. Self-Calibration Bundle Adjustment Method

Bundle adjustment methods are rigorous methods used to solve EO parameters and 3-D ground points simultaneously with high accuracy and consistency. Self-calibration is a common approach to compensate for systematic errors in IO parameters in BA. Systematic errors are usually modeled by several additional parameters and considered as weighted observations to be solved together with other unknowns, thereby self-detecting and eliminating the effect of these errors during the adjustment process. Considering that systematic errors can be conveniently expressed as functions of the image point coordinates, a self-calibration method can be easily conducted in the BA process with image coordinates as observations. Self-calibration methods are mature for stereoscopic earth observation satellites such as ALOS (PRISM) and SPOT5 (HRS) [32]–[35]. However, they are multilens CCD cameras that have different structures from CE-2's single-lens CCD camera. In addition, planetary exploration satellites such as CE-2 CCD camera have the characteristics of low orbit and poor orbit determination accuracy compared with Earth observation satellites. Thus, self-calibration methods for Earth observation satellites may not be completely suitable for CE-2 CCD images.

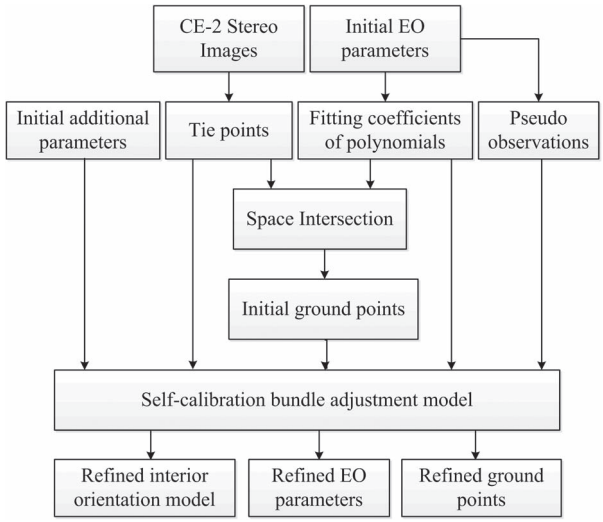

Fig. 4. SCBA method framework for CE-2 CCD images.

In this paper, according to the inconsistency between the two line arrays of CE-2 CCD camera, several additional parameters are introduced into the IO model to describe systematic errors in image space. The original telemetry data are fitted using a polynomial model. Selected telemetry data (with equal intervals) are considered as pseudo-observations to stabilize the SCBA. The adjustment simultaneously refines the IO model with self-calibration parameters, the EO parameters, and the ground points using the image tie points obtained through image matching and the corresponding ground points derived from space intersection and pseudo-observations. Fig. 4 shows the SCBA method framework.

A. Modification on the IO Model

The CE-2 CCD images used in this paper are the Level 2C data with a 7-m resolution in planetary data system (PDS) format [36] released by the National Astronomical Observatories, Chinese Academy of Sciences. These images were acquired at the 100 km $\times$ 100 km circular orbit and preprocessed for radiometric, geometric, and photometric corrections [37]. The acquisition time and the gray values for each scan line can be obtained from the PDS files. Hundreds of evenly distributed tie points are automatically selected using SIFT matching and RANSAC algorithm. Occasionally, a manual tie-point selection may be necessary in certain featureless areas of the images. Three-dimensional ground points and back-projection residuals are calculated by space intersection and back projection. By analyzing the back-projection residuals, we determined that the CE-2 CCD image residuals are significantly larger than those of CE-1 [18], which is likely because of the uncertain relationship between the two CCD camera line arrays, aside from the EO parameter errors.

Therefore, we modified the IO model by adding four additional parameters for forward- and backward-looking images

$$x' = (x - x\_offset)/x\_scale$$
$$y' = (y - y\_offset)/y\_scale \tag{6}$$

where x_offset and x_scale represent the translation and rotation in the x-direction, respectively; similarly, y_offset and y_scale represent the translation and rotation in the y-direction, respectively. The initial values are 0 for x_offset and y_offset and 1 for x_scale and y_scale. These values ensure that the real focal plane coordinate (x', y') is exactly the theoretical coordinate (x, y) in an ideal situation. For a pair of forward- and backward-looking stereo images, there are totally eight self-calibration parameters.

B. Processing of EO Parameters

The original attitude data (the Euler angles from BCS to OCS) were alternately received by two observation stations. When we processed the attitude data, we found that several hours of interruptions occur when neither of the stations observed the orbiter. Attitude data during these interruption periods are difficult to interpolate and estimate precisely. Moreover, we calculated the root-mean-square error (RMSE) of the attitude data for the partial observable period. RMSEs for the three Euler angles are 0.0124°, 0.0087°, and 0.0080°, which do not meet the 0.01° accuracy requirement. Thus, we reset the rotation angles to 0 as initial values in our adjustment method.

1) Polynomial Fitting of EO Parameters: Previous research has shown that the change in the EO parameters of the orbiter over short trajectories can be modeled using polynomials [16], [19], [21]. In this paper, a third-order polynomial model, with the image scan time t as independent variable [as shown in (7)], is used to fit the curve of the EO parameters. Considering that the three Euler angles $(\varphi, \omega, \kappa)$ from BCS to OCS are calculated from ephemeris data $(X_s, Y_s, Z_s, dx, dy, dz)$ and the Euler angles $(\varphi_o, \omega_o, \kappa_o)$ from BCS to OCS, we opt to fit the change of $(\varphi_o, \omega_o, \kappa_o)$ instead of $(\varphi, \omega, \kappa)$ to remove the correlation in the adjustment computation

$$\begin{aligned} X_s(t) &= a_0 + a_1 t + a_2 t^2 + a_3 t^3 \\ Y_s(t) &= b_0 + b_1 t + b_2 t^2 + b_3 t^3 \\ Z_s(t) &= c_0 + c_1 t + c_2 t^2 + c_3 t^3 \\ \varphi_o(t) &= d_0 + d_1 t + d_2 t^2 + d_3 t^3 \\ \omega_o(t) &= e_0 + e_1 t + e_2 t^2 + e_3 t^3 \\ \kappa_o(t) &= f_0 + f_1 t + f_2 t^2 + f_3 t^3 \end{aligned} \tag{7}$$

where $a_0, a_1, \ldots f_3$ are the polynomial coefficients of the six EO parameters $(X_s, Y_s, Z_s, \varphi_o, \omega_o, \kappa_o)$.

It is easy to understand that fitting residuals of EO parameters can become larger as track length increases. Thus, when adjustment is performed in a long track, EO parameters are first divided into several segments and then fitted separately using third-order polynomials to ensure fitting precision. Constraint conditions of continuous first partial derivatives at the junction of two adjacent polynomial curves are also added to the adjustment model.

2) Pseudo-Observation: Given that no ground control is available during the adjustment, the coefficient matrix of the observation equations is rank deficient. Thus, several lines of original EO parameters at certain intervals are selected as pseudo-observations to improve the stability of the observation equations [19]. Given the original EO parameters and the corresponding acquisition time, the observation equations of pseudo-observations can be represented as

$$\begin{aligned} v_{X_s} &= X_s^{\mathrm{ori}}(t) - X_s(t) & v_{\varphi_o} &= \varphi_o^{\mathrm{ori}}(t) - \varphi_o(t) \\ v_{Y_s} &= Y_s^{\mathrm{ori}}(t) - Y_s(t) & v_{\omega_o} &= \omega_o^{\mathrm{ori}}(t) - \omega_o(t) \\ v_{Z_s} &= Z_s^{\mathrm{ori}}(t) - Z_s(t) & v_{\kappa_o} &= \kappa_o^{\mathrm{ori}}(t) - \kappa_o(t) \end{aligned} \tag{8}$$

where $X_s^{\mathrm{ori}}(t), Y_s^{\mathrm{ori}}(t), \ldots, \kappa_o^{\mathrm{ori}}(t)$ are the original EO parameters at time t; $X_s(t), Y_s(t), \ldots, \kappa_o(t)$ are the EO parameters at time t calculated from (7); and $v_x, v_y, \ldots, v_\kappa$ are the corresponding residuals.

C. SCBA Model

According to the general form of collinearity equation in (2) and the modified IO model in (6), the SCBA model can be represented as

$$\begin{aligned} x &= -x\_scale \cdot f \cdot \bar{X}/\bar{Z} + x\_offset \\ y &= -y\_scale \cdot f \cdot \bar{Y}/\bar{Z} + y\_offset \end{aligned} \tag{9}$$

where

$$\begin{aligned} \bar{X} &= a_1(X_A - X_s) + b_1(Y_A - Y_s) + c_1(Z_A - Z_s) \\ \bar{Y} &= a_2(X_A - X_s) + b_2(Y_A - Y_s) + c_2(Z_A - Z_s) \\ \bar{Z} &= a_3(X_A - X_s) + b_3(Y_A - Y_s) + c_3(Z_A - Z_s). \end{aligned}$$

Using Taylor's formula, the linearized observation equations can be derived as

$$\begin{aligned} v_x = {} & \frac{\partial x}{\partial X_S} dX_S + \frac{\partial x}{\partial Y_S} dY_S + \frac{\partial x}{\partial Z_S} dZ_S + \frac{\partial x}{\partial \varphi_o} d\,varphi_o \\ & + \frac{\partial x}{\partial \omega_o} d\,omega_o + \frac{\partial x}{\partial \kappa_o} d\,kappa_o + \frac{\partial x}{\partial X} dX \\ & + \frac{\partial x}{\partial Y} dY + \frac{\partial x}{\partial Z} dZ + \frac{\partial x}{\partial x\_scale} dx\_scale \\ & + \frac{\partial x}{\partial x\_offset} dx\_offset + (x) - x \\ v_y = {} & \frac{\partial y}{\partial X_S} dX_S + \frac{\partial y}{\partial Y_S} dY_S + \frac{\partial y}{\partial Z_S} dZ_S + \frac{\partial y}{\partial \varphi_o} d\,varphi_o \\ & + \frac{\partial y}{\partial \omega_o} d\,omega_o + \frac{\partial y}{\partial \kappa_o} d\,kappa_o + \frac{\partial y}{\partial X} dX \\ & + \frac{\partial y}{\partial Y} dY + \frac{\partial y}{\partial Z} dZ + \frac{\partial y}{\partial y\_scale} dy\_scale \\ & + \frac{\partial y}{\partial y\_offset} dy\_offset + (y) - y. \end{aligned} \tag{10}$$

The whole SCBA model can be then written in matrix form as

$$\begin{aligned} \mathbf{V_M} &= \mathbf{A X_1} + \mathbf{B_1 X_2} + \mathbf{C_1 X_3} - \mathbf{L_1}, \quad \mathbf{P_1} \\ \mathbf{V_{EO}} &= \mathbf{B_2 X_2} - \mathbf{L_2}, \quad \mathbf{P_2} \\ \mathbf{V_{Add}} &= \mathbf{C_2 X_3} - \mathbf{L_3}, \quad \mathbf{P_3} \\ \mathbf{V_{Curve}} &= \mathbf{D X_4} - \mathbf{L_4}, \quad \mathbf{P_4} \end{aligned} \tag{11}$$

where the four equations are the observation equations of tie points, pseudo-observations, additional parameters, and polynomial constraints; $\boldsymbol{X_1}$, $\boldsymbol{X_2}$, $\boldsymbol{X_3}$, and $\boldsymbol{X_4}$ are the unknown corrections of ground points, polynomial coefficients of the EO parameters, additional parameters, and constraints of EO parameters (continuous first partial derivatives), respectively; $\boldsymbol{P_1}$, $\boldsymbol{P_2}$, $\boldsymbol{P_3}$, and $\boldsymbol{P_4}$ are the weights of corresponding equations; $\boldsymbol{A}$, $\boldsymbol{B_1}$, $\boldsymbol{B_2}$, $\boldsymbol{C_1}$, $\boldsymbol{C_2}$, and $\boldsymbol{D}$ are coefficient matrices; and $\boldsymbol{L_1}$, $\boldsymbol{L_2}$, $\boldsymbol{L_3}$, and $\boldsymbol{L_4}$ are constant terms. We did not include absolute control such as LOLA points because we want to exclusively evaluate the potential of CE-2 imagery. The equations in (11) can be combined to form the final SCBA equation in

$$\mathbf{V} = \mathbf{AX} - \mathbf{L}. \tag{12}$$

According to the least squares principle, the normal equation can be presented as

$$\mathbf{A^T PAX} = \mathbf{A^T PL} \tag{13}$$

where $\boldsymbol{P}$ is the weight diagonal matrix comprising $\boldsymbol{P_1}$, $\boldsymbol{P_2}$, $\boldsymbol{P_3}$, and $\boldsymbol{P_4}$ in (11).

Finally, corrections can be calculated using

$$\mathbf{X} = (\mathbf{A^T PA})^{-1}\mathbf{A^T PL}. \tag{14}$$

The adjustment process should iterate until the change in correction value $\mathbf{X}$ is less than the predefined thresholds.

D. Weight Determination

Previous research shows that introducing pseudo-observation equations into adjustment process is an efficient treatment method to adjust any participant contributions flexibly by determining their weights [19], [23]. A reasonable selection of weights facilitates the fast convergence of the solution. Different weights are assigned to different observation types according to our knowledge about their qualities. Weights are assigned using (15) [19]

$$p_i = 1/\sigma_i^2 \tag{15}$$

where p_i and σ_i are the weight and the standard deviation of the ith observation type, respectively.

In this paper, the image tie point measurement standard deviation is half a pixel, which is approximately 3.5 m. According to the position error of orbit determination using Unified S-Band system and Very-long Baseline Interferometry observation data, the perspective center standard deviation (X_s, Y_s, Z_s) is set as 100 m [38], and the pointing angle measurement standard deviation is assumed to be 0.01° [39]. Weights are assigned to these observation equations according to their *a priori* standard deviations. EO polynomial parameter coefficients are adjusted by iteratively solving their weighed observation equations.

As regards the observation equation of additional parameters, a proper weight is determined from the empirical values. The observation equation of EO polynomials is theoretically rigorous with geometric meanings, thus requiring a relatively high weight.

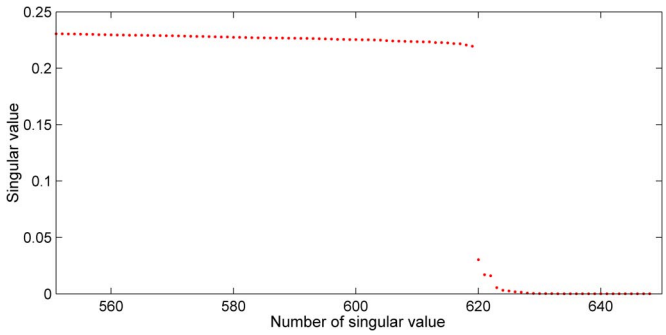

Fig. 5. Singular value distribution pattern.

To avoid the effect of potential errors in tie points, a robust estimation strategy is used in weight determination of the tie points. Since the gross errors in tie points have already been eliminated by the RANSAC strategy, the Huber method is used to mitigate the effect of some little errors [40]. The equivalent weight in this method is determined using

$$\overline{p_i} = \begin{cases} p_i, & |v_i| < k\sigma \\ p_i \frac{k\sigma}{|v_i|}, & |v_i| \geq k\sigma \end{cases} \tag{16}$$

where k is an empirical constant; σ is the RMSE of observations; and v_i and p_i are the residual and weight for the ith observation, respectively. The weight function is divided into two groups, thereby maintaining the weights of normal points while reducing the weights of doubtful points.

In our experiment, weights of different magnitudes around the *a priori* weight for each parameter are tested. The results show that the residuals in both image and object spaces are not sensitive to moderate changes in weight magnitude.

E. Solution of Ill-Posed Equation

The normal equation of an observation equation can be ill posed when the intersection angle of the stereo pairs is extremely small or when correlations exist among unknown parameters. In our experiment, intersection angles between images in the same track and between adjacent tracks are approximately 25.2° and 17.6°, respectively, which form a relatively poor geometric configuration and result in an ill-posed problem in the normal equation of the SCBA model. Thus, we adopt the truncated singular value decomposition (TSVD) method to ensure the stability of the solution. First, singular value decomposition on the coefficient matrix $\mathbf{A^T PA}$ of the normal equation is performed using

$$\underset{m\times n}{\mathbf{A}} = \underset{m\times m}{\mathbf{U}} \times \underset{m\times n}{\mathbf{S}} \times \underset{n\times n}{\mathbf{V}^T} \tag{17}$$

where $\mathbf{U}$ and $\mathbf{V}$ are numeric unitary matrices, the columns of which are the singular vectors, and $\mathbf{S}$ is a diagonal matrix containing the singular values.

We then found that the singular values on the $\mathbf{S}$ diagonal show a step pattern (see Fig. 5). The left side of the "step" has large singular values, which stands for the reliable part of the model, whereas the right part with small singular values stands for the unreliable part to be discarded.

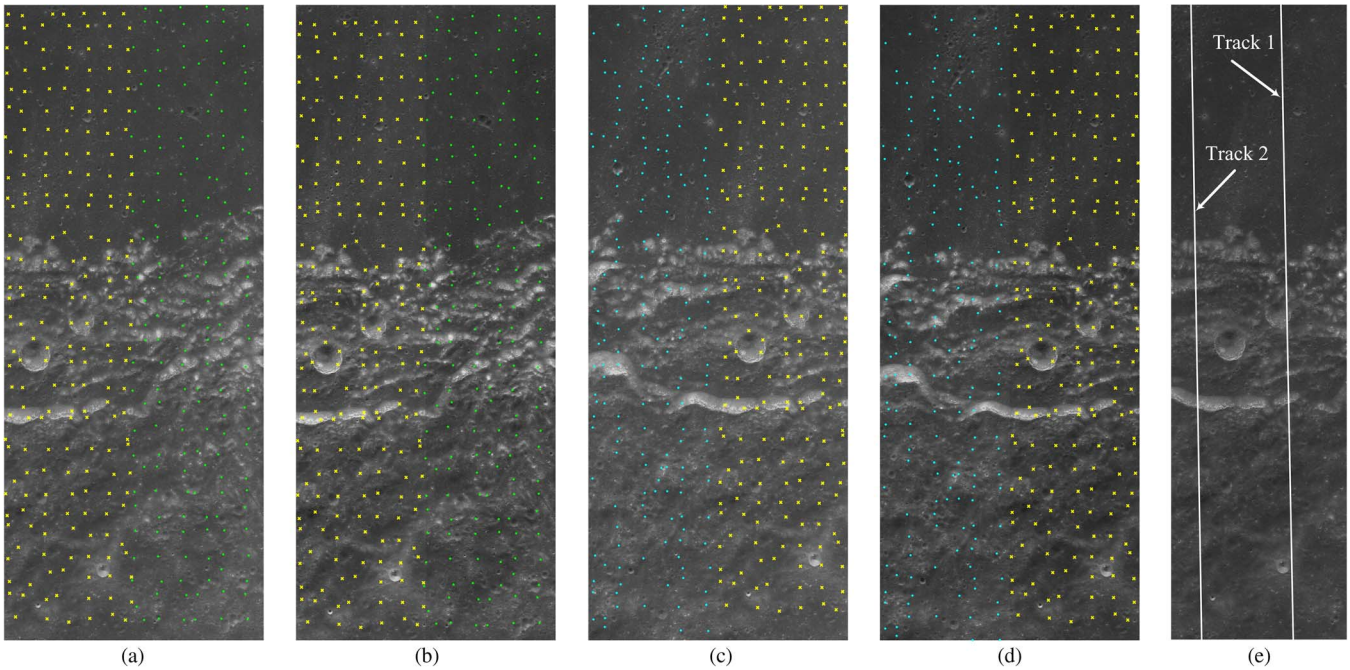

Fig. 6. Partial forward- and backward-looking lunar images (7-m resolution) of the No. 0580 and No. 0581 tracks taken by CE-2 CCD camera: (a) Forward-looking image of No. 0580 track, (b) backward-looking image of No. 0580 track, (c) forward-looking image of No. 0581 track, and (d) backward-looking image of No. 0581 track. Green and blue dots are intratrack tie points; yellow crosses are intertrack tie points. (e) Two selected tracks of LOLA data at Sinus Iridum used for comparison overlaid on the CE-2 CCD image for comparison.

Previous works proved that the TSVD method is applicable to this step-pattern distributed singular value [40], [41]. Thus, the solution to the SCBA equations can be calculated using only the t largest values and their corresponding vectors

$$\mathbf{X} = \underset{n\times t}{\mathbf{V}} \cdot \underset{t\times t}{\mathbf{S}^{-1}} \cdot \underset{m\times t}{\mathbf{U}^{T}} \cdot \underset{n\times 1}{\mathbf{A}^{T}\mathbf{PL}} \qquad (t \le m \quad \text{and} \quad t \le n). \tag{18}$$

IV. Experimental Results

Two tracks (No. 0580 and No. 0581) of CE-2 CCD images located at Sinus Iridum (the CE-3 lunar rover preselected landing site) are used in the experiment. The images were acquired on November 24, 2010 and have a resolution of 7 m. Fig. 6 shows partial forward- and backward-looking images (15 000 rows, after grayscale stretching) of the No. 0580 and No. 0581 tracks.

In our experiment, we used 6144 columns by 15 000 rows of forward- and backward-looking images for both tracks. After image stretching, evenly distributed tie points are automatically selected by SIFT matching with RANSAC-based error elimination. Tie points are of two types, i.e., intratrack points (marked as green and cyan points in Fig. 6) and intertrack points (marked as yellow crosses in Fig. 6). Intratrack points are measured on forward- and backward-looking images from the same track (twofold overlay), whereas intertrack points are measured on forward- and backward-looking images from both tracks (fourfold overlap).

A. Intratrack Adjustment

Initial ground points are calculated by space intersection using forward- and backward-looking images in the same track. The residuals in image space calculated by back projection are shown in Table II, which shows that the back-projection residuals in one track mainly exist in the column direction. Tie points, initial ground points, initial additional parameters, and pseudo-EO observations are then added to the SCBA equations as observations. Table II shows the back-projection residuals for the No. 0580 and No. 0581 tracks before and after self-calibration adjustment. Table III lists the changes of the EO parameters and ground points after adjustment. Additional IO parameters are shown in Table IV. The comparison of adjustment results using traditional method is also listed in Tables II and III. The average of the residuals in the column direction is reduced from more than 5 pixels to subpixel level using the traditional or the self-calibration method. However, by introducing additional IO parameters, the consistency between forward- and backward-looking images can be adjusted without evidently

TABLE II
Back-Projection Residuals Before and After Intratrack Adjustment

	Track No.	Look angle [a]	Column direction (pixel)		Row direction (pixel)	
			Average	RMSE	Average	RMSE
Before Adjustment	0580	F	-5.13	0.46	0.00	0.00
		B	5.13	0.46	0.00	0.00
	0581	F	-5.08	0.46	0.00	0.00
		B	5.08	0.46	0.00	0.00
After Traditional Bundle Adjustment	0580	F	-0.04	0.44	0.00	0.00
		B	0.04	0.44	0.00	0.00
	0581	F	-0.07	0.44	0.00	0.00
		B	0.07	0.44	0.00	0.00
After Self-calibration Bundle Adjustment	0580	F	-0.02	0.43	0.00	0.00
		B	0.02	0.43	0.00	0.00
	0581	F	-0.01	0.42	0.00	0.00
		B	0.01	0.42	0.00	0.00

[a]"F" and "B" in column "Look angle" stand for Forward- and Backward-looking respectively.

TABLE III
CHANGES IN EO PARAMETERS AND GROUND POINTS AFTER INTRATRACK ADJUSTMENT

Method	Track No.	Change for EO parameters		Change for ground points		
		(X_S, Y_S, Z_S) (m)	$(\varphi_O, \omega_O, \kappa_O)$ ($''$)	X (m)	Y (m)	Z (m)
Traditional Bundle Adjustment	0580	31.77	1.20	9.76	15.03	5.83
	0581	30.03	1.07	9.52	13.74	5.17
Self-calibration Bundle Adjustment	0580	4.85	0.13	0.62	0.43	1.18
	0581	5.31	0.16	0.62	0.63	1.31

TABLE IV
ADDITIONAL IO PARAMETERS FOR INTRATRACK ADJUSTMENT

Track No.	Look angle	*x_scale*	*x_offset*	*y_scale*	*y_offset*
0580	F	0.99999999	0.00000052	1.00000198	-0.00005366
	B	1.00000018	0.00000397	0.99999780	0.00005000
0581	F	1.00000000	-0.00000004	1.00000622	-0.00005201
	B	1.00000018	0.00000406	0.99999414	0.00005120

TABLE V
BACK-PROJECTION RESIDUALS BEFORE AND AFTER INTERTRACK ADJUSTMENT

	Track No.	Look angle	Column direction (pixel)		Row direction (pixel)	
			Average	RMSE	Average	RMSE
Before Adjustment	0580	F	-0.61	0.44	20.92	0.51
		B	9.69	0.61	16.72	1.51
	0581	F	-9.53	0.39	-16.84	0.36
		B	1.04	0.79	-20.99	1.42
After Traditional Bundle Adjustment	0580	F	0.06	0.43	0.02	0.24
		B	-0.03	0.42	-0.07	0.65
	0581	F	-0.09	0.44	-0.02	0.33
		B	0.05	0.49	0.05	0.70
After Self-calibration Bundle Adjustment	0580	F	0.04	0.36	0.01	0.13
		B	-0.03	0.40	0.02	0.59
	0581	F	-0.06	0.37	-0.01	0.30
		B	0.04	0.45	-0.04	0.56

changing the terrain (ground points). Since EO parameters for images in one track have a relatively good consistency, slight changes of EO parameters in the self-calibration method are supposed to be more reasonable than the large changes in the traditional method.

B. Intertrack Adjustment

Similar computations are also performed using both intratrack points and intertrack points for intertrack adjustment. Back-projection residuals before and after adjustment are shown in Table V. Changes in EO parameters and ground points are shown in Table VI. For intertrack adjustment, additional IO parameters for different tracks (see Table VII) are considered the same. The self-calibration method slightly outperforms the traditional method. DEMs generated using CE-2 data before and after adjustment are shown in Fig. 7. As shown in Fig. 7, the inconsistencies (e.g., artifacts in the intertrack overlapping area) between two adjacent tracks are effectively eliminated using the two adjustment methods, and the self-calibration method slightly outperforms the traditional method.

TABLE VI
CHANGES IN EO PARAMETERS AND GROUND POINTS AFTER INTERTRACK ADJUSTMENT

Method	Track No.	Change for EO parameters		Change for ground points		
		(X_S, Y_S, Z_S) (m)	$(\varphi_O, \omega_O, \kappa_O)$ ($''$)	X (m)	Y (m)	Z (m)
Traditional Bundle Adjustment	0580	48.98	2.01	7.39	8.87	5.11
	0581	54.17	1.92			
Self-calibration Bundle Adjustment	0580	47.07	1.43	4.08	4.07	8.85
	0581	41.71	1.27			

TABLE VII
ADDITIONAL IO PARAMETERS FOR INTERTRACK ADJUSTMENT

Look angle	*x_scale*	*x_offset*	*y_scale*	*y_offset*
F	0.99999963	0.00000471	1.00026279	-0.00005342
B	0.99999762	-0.00002736	0.99973929	0.00004101

C. Comparison With LOLA Data

To verify the terrain produced from CE-2 data, two tracks of LOLA data are used for comparison. LOLA is a multibeam LAM onboard NASA's LRO. LOLA has a five-spot sampling pattern that can produce five parallel profiles along the LRO's subspacecraft ground track. Profiles are separated by around 10–12 m, and observations within each profile are 56 m apart from one other. The altimetric observations acquired by LOLA have been used to improve the lunar geodetic grid to around 10-m radial and 100-m spatial accuracy values with respect to the Moon's center of mass [43], [44].

In our experiment, the channel one data of two tracks located at our experiment area $(46.62^\circ - 50.13^\circ$ N, $29.04^\circ - 32.57^\circ$ W) is used for comparison and is shown in Fig. 6(e). Detailed information on the two LOLA tracks is listed in Table VIII. After a simple translation, profiles are generated using original and adjusted CE-2 data by interpolating with the longitudes and latitudes of the selected LOLA tracks. The LOLA and CE-2 profiles are visually compared in Fig. 8; two insets are included for detailed comparison. We calculated the detailed statistics of the differences between the profiles that covered the entire range of our experimental area, and the results are listed in Table IX. From the experimental results, we can see that the terrain generated by CE-2 CCD images is generally consistent with that of LOLA data regardless of whether adjustment is performed. SCBA effectively corrects fine-scale local terrain. After adjustment, the elevation differences are reduced by 9–10 m. Overall, the SCBA method shows a slight advantage over the traditional BA method.

It is worth to note that we also tried a different set of self-calibration parameters and found that the proposed eight-parameter model [see (6)] can achieve the best precision with stable solution. Less number of parameters would not be effective to reduce back-projection residuals; more parameters did not provide better results than the eight parameters.

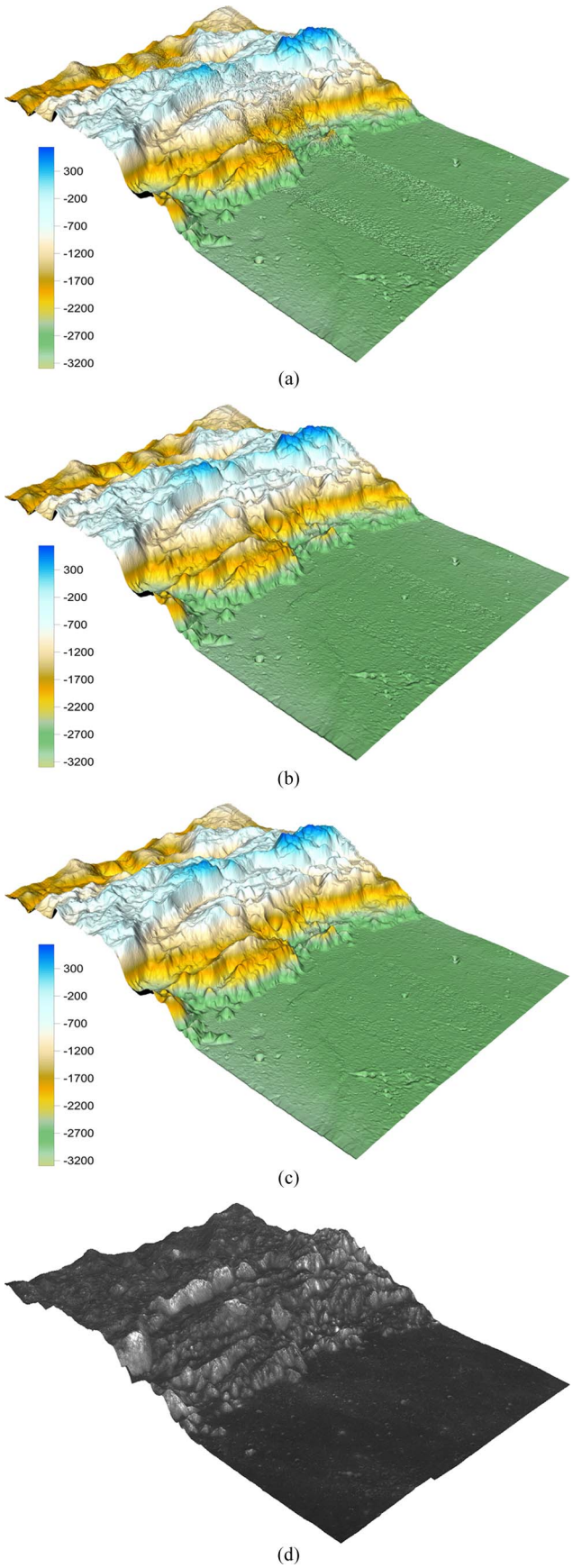

Fig. 7. DEMs of CE-2 CCD images. (a) DEM generated using original CE-2 data. (b) DEM generated using CE-2 data after traditional BA. (c) DEM generated using CE-2 data after SCBA. (d) DOM overlaid on the DEM after SCBA.

TABLE VIII
TWO TRACKS SELECTED FROM LOLA DATA AT SINUS IRIDUM

LOLA Data	Orbit No.	Start Time	End Time	Point Number
Track 1	1957	2009-11-29T 18:21:56.653Z	2009-11-29T 18:23:12.011Z	1822
Track 2	10994	2011-11-09T 10:46:19.830Z	2011-11-09T 10:47:33.973Z	2071

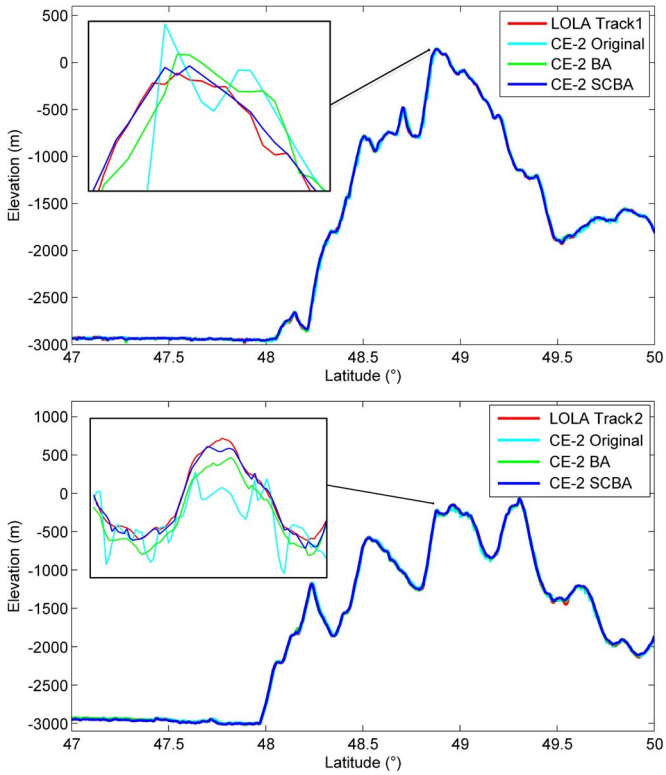

Fig. 8. Profile comparison of two LOLA tracks. "CE-2 Original," "CE-2 BA," and "CE-2 SCBA" represent the profiles before adjustment, after traditional method, and after self-calibration method, respectively.

TABLE IX
STATISTICS OF PROFILE COMPARISONS BETWEEN LOLA AND CE-2 DATA

Track No.	Statistics (m)	Before Adjustment	After Traditional Bundle Adjustment	After Self-calibration Bundle Adjustment
Track 1	Mean	53.07	32.47	31.74
	Maximum	179.56	90.40	83.96
	StdDev	19.92	10.77	9.14
Track 2	Mean	85.32	30.24	28.73
	Maximum	162.76	113.05	94.68
	StdDev	23.44	14.99	14.01

V. CONCLUSION AND DISCUSSION

The rigorous geometric model of CE-2 CCD images has been developed in this paper. After analyzing the cause of inconsistencies between images of different-looking angles in one track and between adjacent tracks, a self-calibration bundle adjustment method is proposed by introducing additional IO parameters to the traditional bundle adjustment model. A series of strategies is used to enhance the stability of adjustment equation, including pseudo-observation selection from EO

parameters, a reasonable weight determination strategy, and the TSVD method for ill-posed equation solutions. Experiments were performed with two tracks of CE-2 CCD images located at Sinus Iridum, and the results showed that the SCBA method was effective in eliminating the inconsistencies of CE-2 CCD images by reducing the image residuals from more than 20 pixels to subpixel level. The accuracy in object space was also verified by comparing the ground points with two tracks of LOLA data. The differences between CE-2 data and LOLA data were reduced by 9–10 m after adjustment. Experimental results also indicated that the SCBA method had a certain advantage over the traditional BA method in terms of the precision improvement in both the image and object spaces.

The proposed SCBA method and the developed geometric processing and mapping procedure are valuable for high-precision lunar topographic mapping using CE-2 images, and the 3-D topographic products can be used for various fine-scale scientific investigations, as well as for the landing preparation and surface operation of the incoming Chang′E-3 lunar rover. In further research, ground control data (e.g., LAM points) will be incorporated into the BA model for stricter constraint and absolute orientation. More images from other sites will be also used to verify the effectiveness of the SCBA method.

ACKNOWLEDGMENT

The authors would like to thank the Lunar and Deep Space Exploration Science Applications Center of the National Astronomical Observatories and Beijing Aerospace Control Center for providing the CE-2 images and telemetry data, respectively.

REFERENCES

[1] S. Nozette, P. Rustan, L. P. Pleasance, D. M. Horan, P. Regeon, E. M. Shoemaker, P. D. Spudis, C. H. Acton, D. N. Baker, J. E. Blamont, B. J. Buratti, M. P. Corson, M. E. Davies, T. C. Duxbury, E. M. Eliason, B. M. Jakosky, J. F. Kordas, I. T. Lewis, C. L. Lichtenberg, P. G. Lucey, E. Malaret, M. A. Massie, J. H. Resnick, C. J. Rollins, H. S. Park, A. S. McEwen, R. E. Priest, C. M. Pieters, R. A. Reisse, M. S. Robinson, R. A. Simpson, D. E. Smith, T. C. Sorenson, R. W. Vorder Breugge, and M. T. Zuber, "The Clementine mission to the moon: Scientific overview," *Sci. New Series*, vol. 266, no. 5192, pp. 1835–1839, Dec. 1994.

[2] J. Haruyama, M. Ohtake, T. Matunaga, T. Morota, C. Honda, Y. Yokota, and Y. Ogawa, "SELENE (KAGUYA) terrain camera observation results of nominal mission period," presented at the 40th Lunar Planetary Science Conf., Houston, TX, USA, Mar. 23–27, 2009, Paper 1553.

[3] A. S. Kiran Kumar and A. Roy Chowdhury, "Terrain mapping camera for Chandrayaan-1," *J. Earth Syst. Sci.*, vol. 144, no. 6, pp. 717–720, Dec. 2005.

[4] Arizona State University, Phoenix, AZ, USA, Reconnaissance Orbiter Camera. [Online]. Available: http://lroc.sese.asu.edu/

[5] Z. Ouyang and C. Li, "The primary science result from the Chang′E-1 probe," *Sci. China Ser. D, Earth Sci.*, vol. 53, no. 11, pp. 1565–1581, Nov. 2010.

[6] C. Li, J. Liu, X. Ren, L. Mou, Y. Zou, H. Zhang, C. Lü, J. Liu, W. Zuo, Y. Su, W. Wen, W. Bian, B. Zhao, J. Yang, X. Zou, M. Wang, C. Xu, D. Kong, X. Wang, L. Fa. Wang, Z. Geng, L. Zhang, X. Zheng, J. Zhu, and Z. Li, "The global image of the Moon obtained by the Chang′E-1 Data processing and lunar cartography," *Sci. China Ser. D, Earth Sci.*, vol. 40, no. 3, pp. 294–306, Aug. 2010.

[7] Z. Ouyang, "Preliminary scientific results of Chang′E-1 lunar probe and missions of Chang′E-2 lunar probe," *Spacecraft Eng.*, vol. 19, no. 5, pp. 1–6, Sep. 2010.

[8] National Astronomical Observatories, Chinese Academy of Science, Release of the first Chang′E-2 image of Sinus Iridum, Nov. 8, 2010. [Online]. Available: http://moon.bao.ac.cn/templates/T_yestem_articelcontent/index.aspx?nodeid=13&page=ContentPage&contentid=184

[9] C. Li, "China publishes the most clear moon map," *Defence Sci. Technol. Ind.*, no. 2, pp. 20–21, Feb. 2012.

[10] J. Oberst, T. Roatsch, W. Zhang, A. C. Cook, R. Jaumann, T. Duxbury, F. Wewel, R. Uebbing, F. Scholten, and J. Albertz, "Photogrammetric analysis of Clementine multi-look angle images obtained near Mare Orientale," *Planet. Space Sci.*, vol. 44, no. 10, pp. 1123–1133, Oct. 1996.

[11] J. Haruyama, S. Hara, K. Hioki, A. Iwasaki, T. Morota, M. Ohtake, T. Matsunaga, H. Araki, K. Matsumoto, Y. Ishihara, H. Noda, S. Sasaki, S. Goossens, and T. Iwata, "Lunar global digital terrain model dataset produced from SELENE (Kaguya) terrain camera stereo observations," presented at the 43th Lunar Planetary Science Conf., The Woodlands, TX, USA, Mar. 19–23, 2012, Paper 1200.

[12] P. V. Radhadevi, V. Nagasubramanian, S. S. Solanki, T. Krishna Sumanth, J. Saibaba, and G. Varadan, "Rigorous photogrammetric processing of Chandrayaan-1 Terrain Mapping Camera (TMC) images for lunar topographic mapping," presented at the 42th Lunar Planetary Science Conf., The Woodlands, TX, USA, Mar. 7–11, 2011, Paper 1384.

[13] T. Tran, M. R. Rosiek, R. A. Beyer, S. Mattson, E. Howington-Kraus, M. S. Robinson, B. A. Archinal, K. Edmundson, D. Harbour, and E. Anderson, "Generating digital terrain models using LROC NAC images," in *Proc. Spec. Joint Symp. ISPRS Tech. Commiss. IV Auto-Carto Conjunction ASPRS/CaGIS Fall Spec. Conf.*, Orlando, FL, USA, Nov. 15–19, 2010, vol. 38, pp. 1–7.

[14] R. Li, W. Wang, S. He, J. W. Hwangbo, Y. Chen, P. Tang, X. Meng, Y. Choung, J. Lawver, P. Thomas, M. Robinson, and M. Rosiek, "Precision photogrammetric modeling of LROC NAC cameras and topographic products," in *Proc. Annu. Meet. Lunar Exploration Anal. Group*, Washington, DC, USA, Sep. 14–16, 2010, p. 36.

[15] R. L. Kirk, L. A. Soderblom, E. Howington-Kraus, and B. A. Archinal, "USGS high-resolution topomapping of Mars with Mars obiter camera narrow-angle images," in *Proc. ISPRS Symp. Geospatical Theory, Process. Appl.*, Ottawa, ON, Canada, Jul. 9–12, 2002, pp. 713–722.

[16] J.-S. Yoon and J. Shan, "Combined adjustment of MOC stereo imagery and MOLA altimetry data," *Photogramm. Eng. Remote Sens.*, vol. 71, no. 10, pp. 1179–1186, Oct. 2005.

[17] H. Ebner, M. Spiegel, A. Baumgartner, B. Giese, and G. Neukum, "Improving the exterior orientation of Mars express HRSC imagery," presented at the Proc. 21st ISPRS Congr., Beijing, China, Jul. 3–11, 2008, pp. 852–857.

[18] R. L. Kirk, E. Howington-Kraus, M. R. Rosiek, J. A. Anderson, B. A. Archinal, K. J. Becker, D. A. Cook, D. M. Galuszka, P. E. Geissler, T. M. Hare, I. M. Holmberg, L. P. Keszthelyi, B. L. Redding, W. A. Delamere, D. Gallagher, J. D. Chapel, E. M. Eliason, R. King, and A. S. McEwen, "Ultrahigh resolution topographic mapping of Mars with MRO HiRISE stereo images: Meter-scale slopes of candidate Phoenix landing sites," *J. Geophys. Res.*, vol. 113, no. E3, pp. E00A24-1–E00A24-31, Mar. 2008.

[19] R. Li, J. Hwangbo, Y. Chen, and K. Di, "Rigorous photogrammetric processing of HiRISE stereo imagery for Mars topographic mapping," *IEEE Trans. Geosci. Remote Sens.*, vol. 49, no. 7, pp. 2558–2572, Jul. 2011.

[20] R. Wang, "EFP bundle triangulation using lunar imagery obtained from satellite three-line-array camera," *Sci. Surv. Mapping*, vol. 33, no. 4, pp. 5–7, Jul. 2008.

[21] M. Peng, Z. Yue, Y. Liu, and K. Di, "Research on lunar and Mars orbital stereo image mapping," in *Proc. SPIE Remote Sens. Environ., 17th Remote Sens. Conf.*, Hangzhou, China, Aug. 27–31, 2010, vol. 8203, pp. 820304-1–820304-8.

[22] K. Di, Z. Yue, M. Peng, and Z. Liu, "Co-registration of Chang′E-1 stereo images and laser altimeter data for 3D mapping of lunar surface," in *Proc. ASPRS/CaGIS 2010 Specialty Conf.*, Orlando, FL, USA, Dec. 15–19, 2010, pp. 1–7.

[23] B. Wu, J. Guo, Y. Zhang, B. A. King, Z. Li, and Y. Chen, "Integration of Chang′E-1 imagery and laser altimeter data for precision lunar topographic modeling," *IEEE Trans. Geosci. Remote Sens.*, vol. 49, no. 12, pp. 4889–4903, Dec. 2011.

[24] K. Di, W. Hu, Y. Liu, and M. Peng, "Co-registration of Chang′E-1 stereo images and laser altimeter data with crossover adjustment and image sensor model refinement," *Adv. Space Res.*, vol. 50, no. 12, pp. 1615–1628, Dec. 2012.

[25] K. Di, Y. Liu, B. Liu, and M. Peng, "Rigorous photogrammetric processing of Chang′E-1 and Chang′E-2 stereo imagery for lunar topographic mapping," in *Proc. 22nd ISPRS Congr.*, Melbourne, Australia, Aug. 25/Sep. 1, 2012, pp. 307–312.

[26] B. Zhao, J. Yang, D. Wen, W. Gao, L. Chang, Z. Song, B. Xue, and W. Zhao, "Overall scheme and on-orbit images of Chang′E-2 lunar satellite CCD stereo camera," *Sci. China Ser. E, Technol. Sci.*, vol. 54, no. 9, pp. 2237–2242, Sep. 2011.

[27] B. Zhao, D. Wen, J. Yang, W. Gao, L. Chang, B. Xue, and Z. Song, "Two bore-sight stereo mapping with single lens, TDI CCD pushing model imaging and compensations of the speed-to-height rate—Chang′E-2 CCD camera," *Acta. Opt. Sin.*, vol. 31, no. 9, pp. 134–141, Sep. 2011.
[28] B. Zhao, J. Yang, D. Wen, W. Gao, L. Chang, and B. Xue, "Chang′E-2 lunar orbiter CCD stereo camera design and validation," *Spacecraft Eng.*, vol. 20, no. 1, pp. 14–21, Jan. 2011.
[29] Y. Xiao, *Principle of Aircraft Flight Dynamics*. Beijing, China: Astronautics Press, 1995, p. 204.
[30] D. G. Lowe, "Distinctive image features from scale-invariant keypoints," *Int. J. Comput. Vis.*, vol. 60, no. 2, pp. 91–110, Nov. 2004.
[31] M. A. Fischler and R. C. Boolles, "Random sample consensus: A paradigm for model fitting with applications to image and automated cartography," *Commun. ACM*, vol. 24, no. 6, pp. 381–395, Jun. 1981.
[32] P. V. Radhadevi, R. Müller, P. d'Angelo, and P. Reinartz, "In-flight geometric calibration and orientation of ALOS/PRISM imagery with a generic sensor model," *Photogramm. Eng. Remote Sens.*, vol. 77, no. 5, pp. 531–538, May 2011.
[33] S. Kocaman and A. Gruen, "Orientation and self-calibration of ALOS PRISM imagery," *Photogramm. Rec.*, vol. 23, no. 123, pp. 323–340, Sep. 2008.
[34] D. Poli, L. Zhang, and A. Gruen, "SPOT-5/HRS stereo images orientation and automated DSM generation," in *Proc. 20th ISPRS Congr.*, Istanbul, Turkey, Jul. 12–23, 2004, vol. 35, pp. 421–432.
[35] P. Michalis and I. Dowman, "A rigorous model and DEM generation for SPOT5–HRS," in *Proc. 20th ISPRS Congr.*, Istanbul, Turkey, Jul. 12–23, 2004, pp. 410–415.
[36] "Planetary data system standards reference," California Inst. Technol., Pasadena, CA, USA, 2002.
[37] National Astronomical Observatories, Chinese Academy of Science, CLEP data description. [Online]. Available: http://159.226.88.59:7779/CE1OutENGWeb/explain.jsp
[38] M. Chen, J. Cao, Y. Zhang, X. Li, G. Tang, J. Wang, J. F. Duan, J. F. Xie, and B. Tong, "Orbit determination and tracking technology of CE-2 satellite," *Chin. Sci. Bull.*, vol. 57, no. 9, pp. 689–696, Sep. 2012.
[39] X. Li, private communication, 2012.
[40] P. J. Huber, *Robust Statistics*. New York, NY, USA: Wiley, 1981.
[41] P. C. Hansen, "Analysis of discrete ill-posed problems by means of the L-curve," *SIAM Rev.*, vol. 34, no. 4, pp. 561–580, Dec. 1992.
[42] Z. Wang and J. Ou, "A new ill-posed singular value correction scheme and the application of geodesic survey," *Prog. Nat. Sci.*, vol. 14, no. 6, pp. 672–676, Jun. 2004.
[43] D. E. Smith, M. T. Zuber, G. B. Jackson, J. F. Cavanaugh, G. A. Neumann, and H. Riris, "The Lunar Orbiter Laser Altimeter investigation on the Lunar Reconnaissance Orbiter mission," *Space Sci. Rev.*, vol. 150, no. 1–4, pp. 209–241, Jan. 2010.
[44] D. E. Smith, M. T. Zuber, G. A. Neumann, F. G. Lemoine, E. Mazarico, M. H. Torrence, J. F. McGarry, D. D. Rowlands, J. W. Head, III, T. H. Duxbury, O. Aharonson, P. G. Lucey, M. S. Robinson, O. S. Barnouin, X. Sun, P. Liiva, D.-d. Mao, J. C. Smith, and A. E. Bartels, "Initial observations from the Lunar Orbiter Laser Altimeter (LOLA)," *Geophys. Res. Lett.*, vol. 37, no. 18, pp. L18204-1–L18204-6, Sep. 2010.

Kaichang Di received the B.Sc., M.Sc., and Ph.D. degrees from the Wuhan Technical University of Surveying and Mapping, Wuhan, China, in 1989, 1990, and 1999, respectively, all in photogrammetry and remote sensing.

He was a Research Scientist with the Department of Civil and Environmental Engineering and Geodetic Science, The Ohio State University, Columbus, OH, USA. He is currently a Professor with the Institute of Remote Sensing Applications, Chinese Academy of Sciences, Beijing, China. His research interests include planetary mapping, photogrammetry and remote sensing, and geographic information systems.

Prof. Di is a cochair of Work Group IV/8 "Planetary Mapping and Spatial Databases" of the International Society for Photogrammetry and Remote Sensing.

Yiliang Liu received the B.E. degree in photogrammetry and remote sensing from Wuhan University, Wuhan, China, in 2009. She is currently working toward the Ph.D. degree in photogrammetry and remote sensing in the Institute of Remote Sensing Applications, Chinese Academy of Sciences, Beijing, China.

Her current research focuses on rigorous geometric modeling of lunar and Mars orbital sensors for high-precision topographic mapping.

Bin Liu received the Ph.D. degree in photogrammetry and remote sensing from Wuhan University, Wuhan, China, in 2011.

He is currently an Assistant Professor with the Institute of Remote Sensing Applications, Chinese Academy of Sciences, Beijing, China. His current research interests include rigorous and generic geometric modeling of high-resolution satellite images and high-precision topographic mapping for Earth observation applications.

Man Peng received the B.S. and M.S. degrees in photogrammetry and remote sensing from Wuhan University, Wuhan, China, in 2003 and 2006, respectively, and the Ph.D. degree from the Chinese Academy of Sciences, Beijing, China, in 2011. Her doctoral research focused on high-precision wide-baseline mapping of the planetary rovers.

She is currently an Assistant Professor with the Institute of Remote Sensing Applications, Chinese Academy of Sciences. Her research interests include planetary exploration, digital mapping, photogrammetry, and remote sensing.

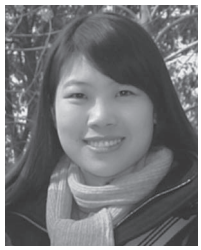

Wenmin Hu received the B.S. and M.S. degrees in photogrammetry and remote sensing from Wuhan University, Wuhan, China, in 2004 and 2006, respectively. She is currently working toward the Ph.D. degree in photogrammetry and remote sensing in the Institute of Remote Sensing Applications, Chinese Academy of Sciences, Beijing, China.

Her research includes lunar and Mars laser altimeter data processing, coregistration of charge-coupled-device images and laser altimeter data.